Electrochromic Performance of Sputtered NbTi-Based Mixed Metal Oxide Thin Films with a Metallic Seed Layer

Karunanithi Balamurugan, Sacratees Santhosh, Mahendran Mathankumar, and Balasubramanian Subramanian*

Cite This: *ACS Omega* 2023, 8, 219−230

Read Online

ACCESS | Metrics & More | Article Recommendations | Supporting Information

ABSTRACT: An attempt has been made to promote the efficiency of the electrochromic (EC) windows to perform at a faster switching rate with good coloration and easy recyclability. In this work, ion-assisted pulsed DC unbalanced confocal magnetron sputtering is used to fabricate mixed metal oxide thin films of Nb and Ti (which are termed as NTO) for EC applications. Further, to increase the EC efficiency of this film, a very thin metallic seed layer is incorporated between the substrate and the film using the layer-by-layer (LBL) coating strategy. The film was prepared by two steps: (i) very thin metallic seed layer coating and (ii) mixed metal oxide NTO layer coating. The metal layer was made of a Nb metal, Ti metal, and NbTi mixed metal, which was coated with the substrate and NTO layer, resulting in three different films, namely, Nb-NTO, Ti-NTO, and NbTi-NTO. The EC properties of these three films were studied in 1 M $LiClO_4$ dissolved in propylene carbonate and

compared with the as-prepared NTO film. The results showed that the Nb-NTO film showed better EC properties, fast switching, better stability, and good recyclability. To check the stability, the film was subjected to prolonged cycling of 500 cycles with a harsh anodic and cathodic sweep at the scan rate of 100 mV s^{-1}. The UV−Vis spectrum confirmed the Li^+ trapping in the films after prolonged cycling. To detrap the ions from the host surface, galvanostatic detrapping is carried out called rejuvenation studies. The rejuvenation rate of films is studied at a constant current loading of ∼2 × 10^{-5} A cm^{-2}. To check the commercialization of the EC window, we successfully fabricated the Nb-NTO device with a PEO-$LiClO_4$-based polymer gel electrolyte.
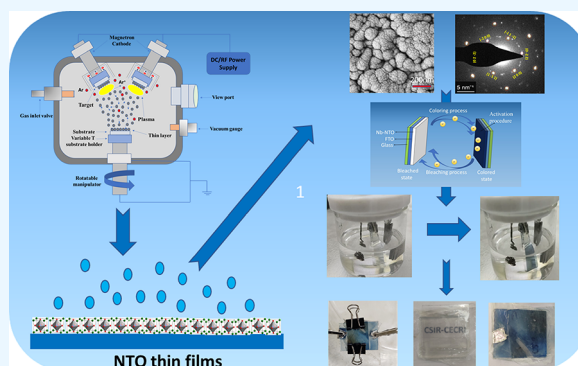
1. INTRODUCTION

Efficient electrochromic materials play an important role in increasing the efficiency of the window by reducing power consumption usage.[1,2] Electrochromism is the phenomenon of changing the optical modulation by applying an external potential during an electrochemical reaction.[3,4] Electrochromic materials have attracted greater attention toward the application of display devices, antiglare windows, electrochromic windows, sunglasses, and smart windows. Most of the traditional electrochromic devices modulate the visible light from the solar spectrum. Recent research on electrochromic devices shows that they can act as a dual-band regulator of heat and light. Coupling the traditional electrochromic materials with the nanostructured material could improve the window's efficiency by regulating the building's energy consumption.[1−5] Among different materials, transition metal oxides (TMOs) like TiO_2, WO_3, MoO_3, Nb_2O_5, and V_2O_5 and conjugated polymers (CPs) like polyaniline, polypyrrole, and polythiophene are often studied. Among them, TMOs are most widely used in electrochromic windows due to their stability and the availability of colors. TMOs play an important role in science and technology as color control can be done at any time; this

operation could be done by changing the valence state of the lattice by reversible intercalation and de-intercalation of Li^+, H^+, and Na^+.[6−8] It is perceived from the fundamental principles and literature review regarding electrochromism that the earth has abundant as well as long-term stable electrodes, which is necessary for the future. The fabrication of thin films for the electrochromic applications was done in different strategies, but the incorporation of the metal layer with the semiconducting layer has been studied by fewer so far. TMOs and CPs with electrochromic properties used for the device application naturally performed well, and charge and carrier transport plays an essential role in improving the coloration efficiency of the film.[8] Designing the film with the heterostructure interface is an efficient and facile route to
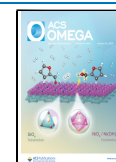
improve the performance by intrinsically affecting the redox states and increasing the catalytic active sites.[9−14]

As in the earlier reports, the improvisation of functional materials in devices was mainly due to the fabrication methods and the technologies used to develop the assembly of the electrodes (EC layers) for their significant performance.[15] It was observed from previous studies by Cai et al. who fabricated different high-performing EC films with different methods by varying the switching times, and color contrast would increase the performance of the electrochromic device.[16,17] A review reported by Richardson et al. focused on the fabrication of the assembly of EC layer by the LBL method to enhance EC performance by controlling the thickness of the layers.[18] But the problem in fabricating a nanoparticle-based layer-by-layer film and fabrication of the film by screen printing is adhesion. In addition to that, the available fabrication techniques are slow and lack uniformity to suit industrial needs.[19] The benefits of adding different elements as a seed layer are to improve the conductivity and the efficiency of the electrochromic application. In this study, the Nb metallic seed layer improves the efficiency of the application by its highly conductive nature, which significantly enhances the application's performance. The as-fabricated pristine film without a seed layer shows higher resistance than other samples. While adding the seed layer, the conductivity of the film increases and also it enhances the efficiency of the electrochromic behavior. In the case of adding a seed layer of Nb, it enhances the electrochromic efficiency of the NTO film more than the other samples. While adding the Ti metallic layer and NbTi metallic layer, the efficiency of the electrochromic behavior is lesser than that of the Nb-NTO film, clearly indicating that Nb is more conductive in nature than Ti and NbTi.

To improve the efficiency of the film, a metallic seed layer was added to FTO because of its low conductive nature and the need for a transparent electrode for smart windows. When we go for the EC efficiency of the electrode/electrolyte interface of NTO film without a seed layer, it does not show high efficiency. With the addition of a seed layer, it improves the electrode/electrolyte interface of Nb-NTO, and the Ti-NTO electrode significantly enhances its performance by its highly conductive nature.

To overcome the drawbacks, precise control over the fabrication double target sputtering technique was used to fabricate the metallic layer, and the mixed metal oxide layer was used to establish this work. Mixed niobium and titanium oxide (NTO) films were initially fabricated and subjected to electrochemical studies. To enrich the film's coloration, incorporating a metallic seed layer has been carried out using ion-assisted pulsed DC unbalanced confocal magnetron sputtering. A facile layer-by-layer strategy is followed to increase the coloration efficiency of the film. The films fabricated using this LBL technique with a niobium metallic layer followed by NTO were named as Nb-NTO, those with a titanium metallic layer followed by NTO were named as Ti-NTO, and those with a niobium-titanium mixed metallic layer followed by NTO were named as NbTi-NTO. The electrochemical properties of these films were studied and compared with a bare NTO film. Optical modulation of the film before and after intercalation was recorded to check the changes that occurred during seed layer incorporation. To check the stability, cycling was carried out for a period of 500 cycles; after cycling, galvanostatic rejuvenation was carried out to detrap the ions on the host surface.

2. EXPERIMENTAL SECTION

2.1. Fabrication of Thin Films. Among different PVD methods for the fabrication of thin films, ion-assisted pulsed DC unbalanced confocal magnetron sputtering (HINHIVAC, Bangalore, India) plays a vital role in film architecture. So, this method was adopted for the fabrication of thin films. The Ti and Nb target was purchased from Kurt J. Lesker Co. (99.9% pure and 2.00″ diameter × 0.250″ thick), and it was used to fabricate thin films. The schematic diagram representing the fabrication of thin films by ion-assisted pulsed DC unbalanced confocal magnetron sputtering is shown in Figure S1. The targets are installed in the suitable target holders in the instrument. A well-cleaned fluorine-doped tin oxide (FTO)-coated glass plate was used as a substrate obtained from Alfa Aesar Co. The optimized distance between the target and substrates was maintained at 7 cm. The vacuum chamber was first evacuated up to 10^{-6} mbar using an Edwards turbo molecular pump (make Germany). To achieve uniform coating, the substrates were rotated using programmed actuators, and the coatings were carried out at room temperature, i.e., no substrate heating was set. The surface contaminants on Ti and Nb targets were removed by presputtering under an argon atmosphere for 5 min. During the sputtering process, the high-energy argon ions collide on the metal target, and metal ions are ejected out of the target with enough kinetic energy to reach the substrate. An optimized operating power of 200 W was used to eject the target material. Then, pure oxygen gas (99.9%) was introduced into the chamber so that the pressure in the chamber was maintained at ~10^{-3} to 10^{-2} mbar to attain metal oxide coating. The layer-by-layer coating strategy was followed during metallic seed layer incorporation. Finally, obtained thin film samples are represented as NTO, Nb-NTO, Ti-NTO, and NbTi-NTO for further analyses.

2.2. Structural and Morphological Characterizations. The phase identification and crystal structure of the NTO, Nb-NTO, Ti-NTO, and NbTi-NTO thin film electrodes were studied by XRD using a Bruker D8 Advance with Cu Kα radiation (λ = 0.154 nm) at a scan rate of 4°/min. The modes of vibration and structural characterizations of all electrodes were investigated by laser Raman spectroscopy (Labram, HR Horiba) with a laser wavelength of 532 nm (diode laser) (Oxxius), which gives a decisive resolution of 1 cm^{-1}. The elemental and chemical composition and binding energy of all thin film samples were examined by X-ray photoelectron spectroscopy (ESCALAB 250xi, Thermo Scientific). The energy-dispersive X-ray spectrum, nanostructured morphologies, and cross-sectional images of the thin film electrodes were depicted by field emission scanning electron microscopy (FESEM; Carl Zeiss, SUPRA 55VP), and the topographical images and roughness profile were examined by Fourier transform infrared spectroscopy (Agilent Technologies, 5500 series). The nanostructured morphologies, lattice fringes, and selected area electron diffraction (SAED) patterns were ascertained using high-resolution transmission electron microscopy (HRTEM; FEI Tecnai G2 F20) working at an accelerated voltage. The optical and transmittance studies of all thin films were elucidated by a UV−Vis spectrometer (UNICO model: 4802).

2.3. Electrochemical Characterizations. All fabricated NTO, Nb-NTO, Ti-NTO, and NbTi-NTO thin films were subjected to electrochromic studies using a conventional three-
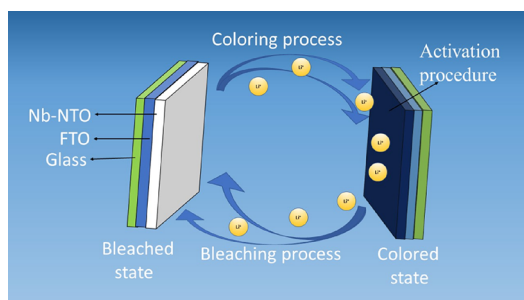
electrode system with as-prepared films as working electrodes, Ag wire as a reference electrode, Pt foil as a counter electrode, and 1 M lithium perchlorate ($LiClO_4$) dissolved in propylene carbonate (PC) as an electrolyte. Cyclic voltammetry (CV) was recorded for all the samples at the sweep rate of 50 mV s^{-1}. The stability of all the films was analyzed with the accelerated degradation (AD) test under a higher scan rate of 200 mV s^{-1} for 500 cycles. Chronoamperometry (CA) studies were carried out to check the switching time, amount of ions involved in the intercalation and de-intercalation process, etc. Galvanostatic detrapping was carried out after prolonged cycling. All electrochemical analyses were carried out in an Ar atmosphere.

2.4. Solid-State Gel Electrolyte Preparation. To fabricate the electrode for commercialization, the Nb-NTO electrode was fabricated as a device, and the corresponding electrode was tested for color change. The gel electrolyte used in the electrochromic device preparation was prepared using the sol−gel method. Five grams of polyethylene oxide powder (PEO) ($\sim 5 \times 10^{-5}$) was dissolved in 90 mL ethylene nitrile (EN) solution and heated at 110 °C with continuous stirring until the solution became translucent for 30 min. Lithium perchlorate powder (5.3 g) was dissolved in propylene carbonate solution. Then, the $LiClO_4$ premixed solution was subsequently added drop by drop with the PEO-EN mixture slowly at a weight ratio of 1:2. The PEO-$LiClO_4$ combination was stirred continuously until a clear solution was attained. The PEO-$LiClO_4$ combination membrane was used in the electrochromic device.

3. RESULTS AND DISCUSSION

The fabricated films named as NTO, Nb-NTO, Ti-NTO, and NbTi-NTO were prepared by the controlled layer-by-layer growth technique using confocal ion beam sputtering in which the atoms from the target (material to be coated as taken in the form of the highly dense pellet) are bombarded by the high energy ions and allowed to reassemble on the substrate. A film with a unique property was grown as a result of the combined effect of reactive gas interactions, mixing atoms, creating bonds, overlapping energy bands, etc. The properties were analyzed, and the reason for the change in the properties is justified here in Figure 1.

3.1. Structural Analysis. The crystallographic information of thin films coated on an FTO substrate was investigated using X-ray diffraction (XRD) at a scan rate of 5°/min. Figure S2 shows the comparative XRD patterns of fabricated thin films, and it is clearly observed from the studies that the films are amorphous to X-rays. The peaks observed in Figure S2 are

substrate peaks indicated by the symbol "#". As reported by Liu et al.,[34] the deposited thin films via the sputtering technique are amorphous in XRD analysis; crystalline grains were observed in the sample, and the sample was crystalline in HRTEM analysis too. A similar observation was made by Thanka Rajan et al.,[32] in which the glassy film fabricated by the sputtering technique was amorphous to X-rays and crystalline in HRTEM analysis. Mathankumar et al.[31] reported that the film fabricated by the pulsed laser deposition technique (PLD) at various oxygen partial pressures did not show any peaks in XRD analysis, but in microscopy analysis, the sample was highly crystalline in nature.

Further, the uniformity of the samples was confirmed by FESEM and AFM analyses, in which the morphological and topographical patterns of the fabricated film support HRTEM results. The FESEM results also proved that the fabricated thin films were grown as nanocrystalline films, and the corresponding images are given in Figure 2 and Figure S3a−c. Among the four different fabricated thin films, Nb-NTO showed high electrochromic efficiency, which was given in the electrochemical analysis, and the corresponding FESEM images of the Nb-NTO thin film with different magnifications are shown in Figure 2. FESEM analysis was also performed for the fabricated films of Ti-NTO, NbTi-NTO, and NTO, and images are shown in Figure S3a−c. The morphology clearly shows that the thin films are composed of numerous tiny crystals of very small grains. We measured the grain size in the fabricated films of NTO, Nb-NTO, Ti-NTO, and NbTi-NTO. The thickness of the seed layer was measured using cross-sectional FESEM analysis, and the thickness of the seed layer was around 34.7 nm. The thickness of the NTO layer was around 346.9 nm. The cross-sectional images are given in Figure S3d, and this shows clear evidence for the formation of the seed layer of around 34 nm; the impact of nanometer seed layer formation is significantly enhancing the coloration of the fabricated film. The measured values are shown in the figure, confirming that the grain size was around 20−40 nm, calculated from the FESEM images using ImageJ or Image Pro Plus software. The thickness of the fabricated thin film is approximately 380 nm, as observed from cross-sectional FESEM images given in Figure S3d. In addition, the seed layer's thickness was calculated using the FESEM cross section, as shown in Figure S3d. Further, topographical patterns of Nb-NTO samples were analyzed using AFM analysis, and the corresponding images are shown in Figure S4. The grain size of the film was uniformly distributed, and the root mean square value of film roughness was around 2.81 nm. AFM images support the FESEM result, which shows a smaller nanosize.

The elemental confirmation and their band nature were evaluated by Raman analysis, which was carried out for all four films, and the comparison spectrum is shown in Figure S5. The high-intensity peaks observed at 117.5, 237.7, 311.1, 690, and 641.2 cm^{-1} correspond to the vibrational energy of the niobium−oxygen bond phase, whereas the peaks observed at the vibrational mode of 685 cm^{-1} and the peak observed for other modes at 311.1 cm^{-1} correspond to the tetragonal phase, which was in good agreement with the XRD analysis. The peaks due to Raman active lattice vibrations observed at 144.6, 197.2, 393, 513.8, and 610 cm^{-1} correspond to the titanium−oxygen bond's vibrational energy. The presence of the most substantial peak at 144.6 is ascribed to crystalline TiO_2. The films show broad peaks, which clearly correspond to the presence of both Nb−O and Ti−O. The Raman spectrum

Figure 1. Schematic representation of the basic color change mechanism in the NTO film during the negative potential sweep.
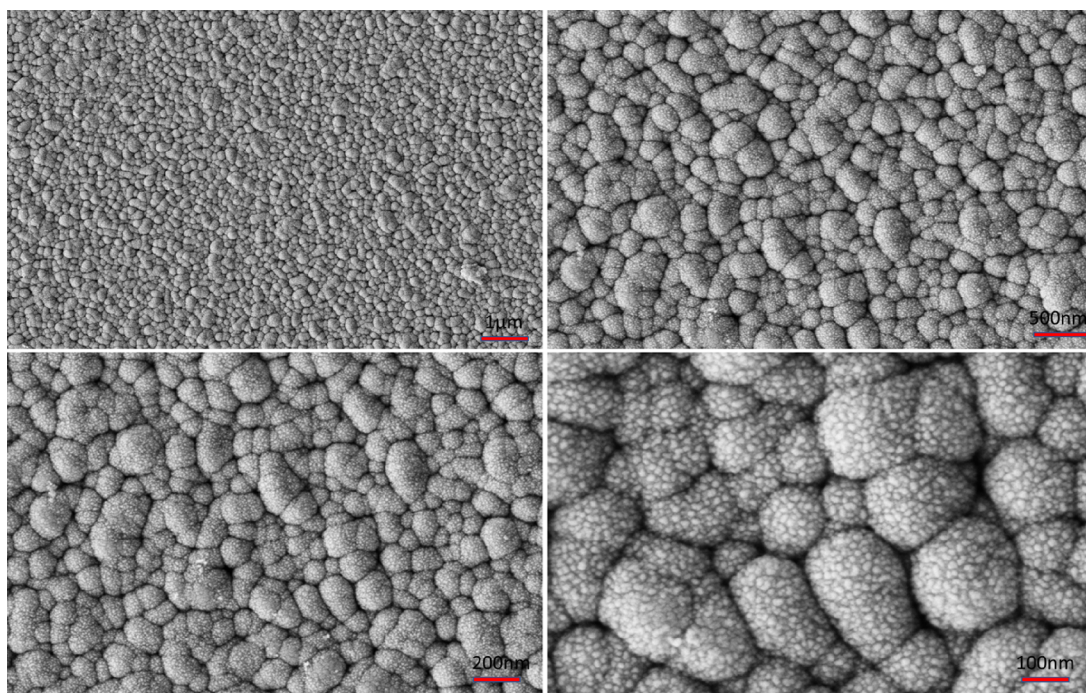
Figure 2. FESEM images of the Nb-NTO thin film with different magnifications.
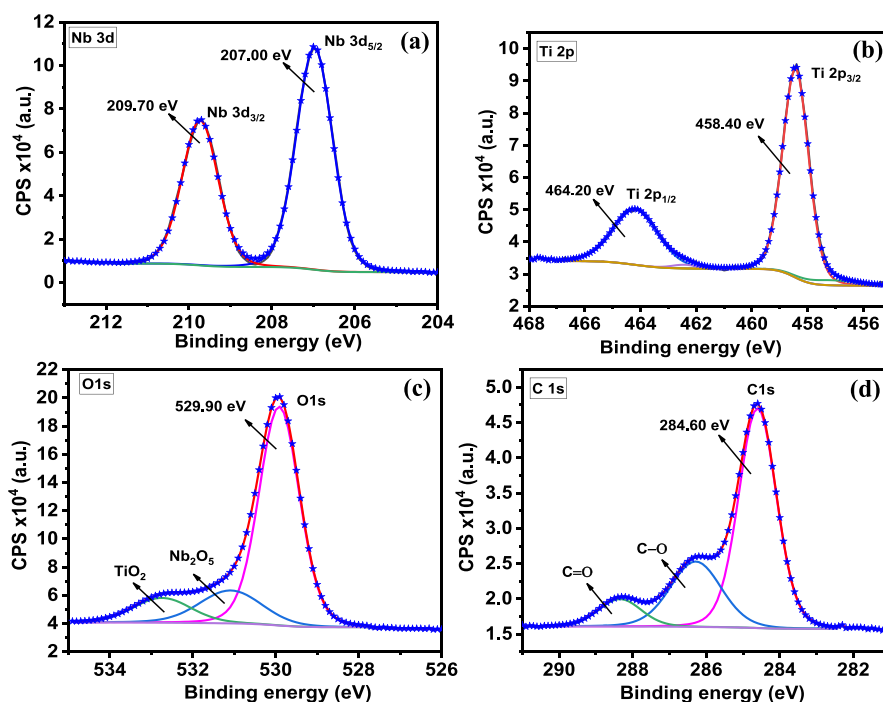

Figure 3. High-resolution XPS spectra of the Nb-NTO film: (a) Nb 3d, (b) Ti 2p, (c) O 1s, and (d) C 1s.

clearly shows that there is not much difference in the peak pattern, and positions confirm that the Raman scattered light from the films is mainly from the film's surface, giving surface information alone. But the careful analysis of the same Raman spectrum clearly revealed that the full width at half maximum of the peaks was unique for all samples. From this, it was concluded that the incorporation of the metal seed layer affected the band nature of the materials present in the film. This creates curiosity to confirm the change in band structure

with proper investigation. So, XPS analysis was utilized to verify the results observed from the Raman spectrum.

To check the elemental analysis and oxidation state of the sample, XPS analysis was carried out. The fabricated films were calibrated with the carbon 1s spectrum, and the position of the peaks was inferred with the NIST XPS database. After carbon corrections, the corresponding spectra are deconvoluted and given in Figure 3. Figure 3 shows the high-resolution XPS spectra of (a) Nb 3d, (b) Ti 2p, (c) O 1s, and (d) C 1s of the Nb-NTO film. The observed spectrum confirms the presence
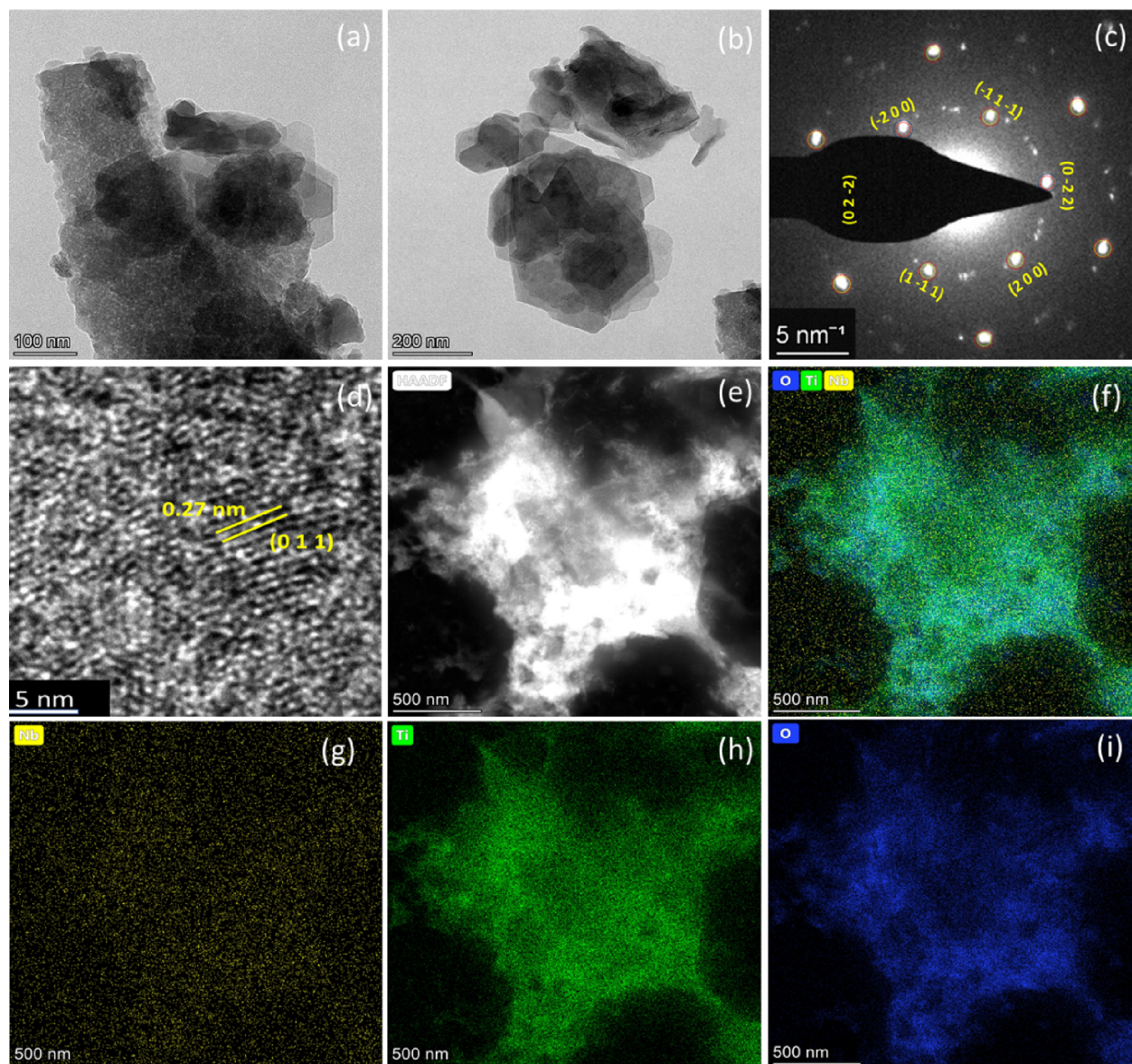
Figure 4. HRTEM images of Nb-NTO films. (a, b) High- and low-magnification bright-field images of Nb-NTO, (c) corresponding indexed diffraction pattern, (d) corresponding indexed lattice fringes, and (e–i) high angle annular dark field (HAADF) analysis of Nb-NTO. Elemental color mapping clearly indicates the presence of Nb, Ti, and O.

of the metallic seed layer, which clearly shows the successful seed layer formation.

Figure 3a shows the deconvoluted high-resolution spectrum of niobium (Nb); the peaks were deconvoluted into two peaks at 209.70 and 207 eV, which correspond to $3d_{3/2}$ and $3d_{5/2}$ of the Nb-NTO-Nb^{V+} state. Figure 3b shows the deconvoluted high-resolution spectrum of Ti 2p, deconvoluted into two peaks at 464.20 and 458.40 eV, corresponding to $2p_{1/2}$ and $2p_{3/2}$. The corresponding O 1s peaks at 529.90 eV and deconvoluted peaks at 531.10 and 532.90 eV are shown in Figure 3c. Figure 3d shows the corresponding deconvoluted C 1s spectrum peaks at 284.60 eV of Nb-NTO.

Figures S6–S8 show the high-resolution XPS spectra of Ti-NTO, NbTi-NTO, and NTO films; the corresponding spectra of Nb 3d, Ti 2p, O 1s, and C 1 s were deconvoluted. Meanwhile, Figures S6 and S7 show the successful seed layer formation Ti and NbTi. Figure S6a shows the deconvoluted niobium spectrum (Nb), which corresponds to $3d_{3/2}$ and $3d_{5/2}$

of the Ti-NTO-Ti^{IV+} state at 209.70 and 207 eV. Figure S6b shows the deconvoluted XPS spectrum of Ti 2p into two peaks at 464.20 and 458.40 eV, which correspond to $2p_{1/2}$ and $2p_{3/2}$. The corresponding O 1s peaks at 529.90 eV deconvoluted peaks at 531.10 and 532.90 eV are shown in Figure S6c. Figure S6d shows the deconvoluted spectrum of C 1s at 284.60 eV of the Ti-NTO thin film. Figure S7a shows the deconvoluted high-resolution spectrum of niobium (Nb) Nb^{V+} at 209.70 and 207.02 eV, corresponding to $3d_{3/2}$ and $3d_{5/2}$ of NbTi-NTO. Figure S7b shows the deconvoluted spectrum of Ti 2p at 464.20 and 458.40 eV, corresponding to $2p_{1/2}$ and $2p_{3/2}$, which show that the fabricated film is at the Ti^{4+} state. The corresponding O 1s peaks at 530, 530.60, and 531.76 eV were deconvoluted, and they are shown in Figure S7c. Figure S7d shows the corresponding deconvoluted C 1s spectrum peaks at 284.80 eV of the NbTi-NTO thin film.

Figure S8 shows the high-resolution XPS spectra of the pristine NTO film in which the elements of (a) Nb 3d, (b) Ti

2p, (c) O 1s, and (d) C 1s were analyzed. Figure S8a shows the deconvoluted spectrum of niobium (Nb); the peaks at 209.70 and 207 eV correspond to $3d_{3/2}$ and $3d_{5/2}$ of NTO. Figure S8b shows the deconvoluted XPS spectrum of Ti 2p; the peaks at 464.10 and 458.30 eV correspond to $2p_{1/2}$ and $2p_{3/2}$. The O 1s peak was deconvoluted into three peaks at 530.20, 531, and 532.80 eV, as shown in Figure S8c. Figure S8d shows the deconvoluted C 1s spectrum; the peaks at 284.80 eV correspond to the pristine NTO thin film.

It was observed from the analysis that the successful seed layer formation had not affected the binding energy of the corresponding NTO, Nb-NTO, Ti-NTO, and NbTi-NTO spectra due to the layer-by-layer formation. Improvement of the electrode efficiency was further reflected due to the LBL formation observed. The atomic ratio of Nb_2O_5, TiO_2, O, and C was calculated from the deconvoluted images, and corresponding relative sensitive factors and areas were obtained from CASA XPS software. The elemental ratio of the efficient film (Nb-NTO) is calculated, and the percentages are as follows: Nb_2O_5, 31.54%; TiO_2, 19.69%; O, 38.23%; C, 10.52%. These XPS results clearly support the results obtained from Raman spectroscopy, which is the alteration of the material's band structure due to seed layer incorporation.

To confirm further with the XRD analysis, HRTEM analysis was carried out to confirm the crystallinity/amorphous nature of the fabricated film and also to observe the microstructure of the thin film. The HRTEM images are shown in Figure 4. The low- and high-magnification images, diffraction patterns, bright-field (BF) images, and fringes are clearly shown in Figure 4. Figure 4a,b shows the bright-field images of the Nb-NTO film, and corresponding figures clearly show the faceted crystal structure. Figure 4c shows the SAED patterns of the Nb-NTO film. The indexed diffraction pattern yields both the ring and spot with 6-fold symmetry. This was indexed and well matched with the tetragonal crystal structure of Nb-NTO, and its corresponding (hkl) values are (−2 0 0), (0 −2 2), and (1 −1 1). It is clearly observed from the diffraction pattern that the films are crystalline; this is due to the nanocrystalline nature of the film, whereas the fabricated films are amorphous to X-rays. As reported by Liu et al.,[34] deposited thin films via the sputtering technique are amorphous in XRD analysis; crystalline grains were observed in the sample, and the sample was crystalline in HRTEM analysis too. A similar observation was made by Thanka Rajan et al.,[32] in which the glassy film fabricated by the sputtering technique was amorphous to X-rays and crystalline in HRTEM analysis. Mathankumar et al.[31] reported that the film fabricated by the pulsed laser deposition technique (PLD) at various oxygen partial pressures did not show any peaks in XRD analysis, but in microscopy analysis, the sample was highly crystalline in nature. Figure 4d shows the indexed diffraction fringes of Nb-NTO, which were well matched and indexed with the corresponding (hkl) value of (011) and fringe width of about 0.27 nm. Figure 4e–i shows the high angle annular dark field (HAADF) analysis of Nb-NTO; elemental color mapping clearly shows the presence of Nb, Ti, and O. The corresponding HAADF image clearly shows the presence of Nb-NTO and also clearly confirms that there is no other impurity present in the sample. Further, it also ensures the uniformity of the sample.

3.2. Electrochemical Characterization. To check the electrochemical properties of the fabricated thin films by LBL fabrication techniques, the fabricated films were subjected to cyclic voltammetry (CV), chronoamperometry (CA), and galvanostatic rejuvenation studies. From the cyclic voltammogram, it is easy to find the electrochemical reaction's nature: reversible or irreversible. Also, the CV curve helps to identify the switching potential for further device design.[20,21] Chronoamperometric studies help to find the electrochemical reaction kinetics; CA data gives the coloration and bleaching time of the film. This coloration and bleaching time are calculated using the standard procedure, i.e., the time taken by the film to attain 70% transformation from its initial stage. It is the key factor considered during device design. The best EC device should be very instantaneous with the applied direction of the potential sweep. Another significant factor for the EC device is its reversibility. This parameter indirectly helps to determine the stability of the device.[22−26] Reversibility is the ratio between the amount of Li^+ ions de-intercalated and the amount of Li^+ ions intercalated into the film during the EC reaction. Practically, it can be calculated either by taking the direct value of the chronocoulometry curve or by finding the area (integrating) of the chronoamperometric curve on both coloration and bleached state. The area under the coloration curve gives the amount of Li^+ intercalated into the film, whereas the area under the bleaching curve gives the amount of Li^+ de-intercalated from the film.[27,28]

The cyclic voltammetry studies were carried out with a potential sweep from −2.5 to 2.5 V vs Ag/AgCl at the scan rate of 50 mV s^{-1} in 1 M $LiClO_4$ dissolved in propylene carbonate. Figure 5 shows a cyclic voltammogram, and Figure 6 shows the
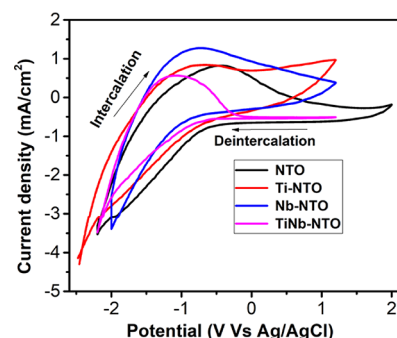
Figure 5. Cyclic voltammetry curves of NTO, Nb-NTO, Ti-NTO, and NbTi-NTO films.

chronoamperometric results of NTO, Ti-NTO, Nb-NTO, and NbTi-NTO films. EC properties of films are shown in Table 1, in which all films show a unique response with the color transition from transparent to blue during the cathodic sweep and vice versa, and the corresponding color change mechanism is represented in the schematic diagram as shown in Figure 1. An electrochromic response was demonstrated and uploaded along with the paper as a video. To check the color change, cyclic voltammetry studies were performed in which niobium and titanium show cathodic coloration. According to the double insertion model, the cathodic EC material gives coloration during lithium-ion (Li^+) insertion, resulting in bronze (Nb and Ti) formation.[29,30] During intercalation and de-intercalation of Li^+, the variation in the current was recorded.

In the case of bare NTO, the working potential window is in the range from −2 to +2 V vs Ag/AgCl, and the coloration happened at a negative potential sweep. The electrochromic switching times of the film were calculated from the chronoamperometry curve, and they were found to be 0.09 s
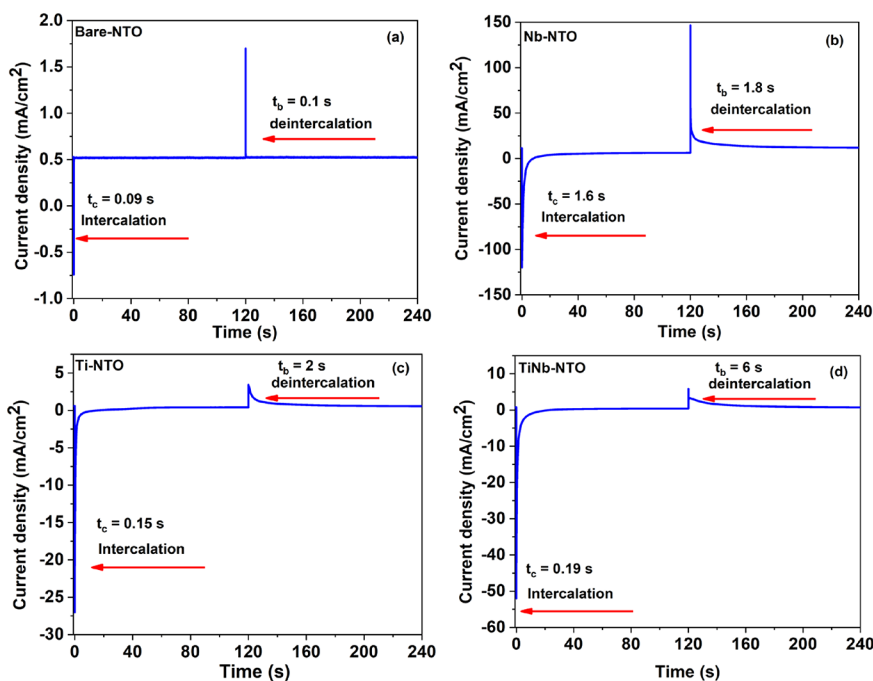
Figure 6. Chronoamperometry spectrum of (a) NTO, (b) Nb-NTO, (c) Ti-NTO, and (d) NbTi-NTO films.

Table 1. Calculated Electrochemical Parameters of Thin Films from Electrochemical and Optical Studies

sample ID	optical modulation (%)	electrochromic kinetics		reversibility (%)	electrochromic efficiency (cm^2/C)
		coloration time t_c (s)	bleaching time t_b (s)		
bare NTO	7	0.09	0.1	10	7.23
Ti-NTO	41	0.15	2	49	36.14
Nb-NTO	57	1.6	1.8	86	72.01
NbTi-NTO	45	0.19	6	54	53.12

for coloration and 0.1 s for bleaching. The reversibility is merely 10%, and the efficiency is about 7.23 cm^2/C, which is not a remarkable value. So, to improve the EC properties, the metallic seed layer is introduced in between the substrate and the NTO film. The EC response of the NTO film with different metallic seed (Ti, Nb, and NbTi) layer incorporation is as follows.

Ti-NTO is found to work in the range of −2.5 to 1 V vs Ag/AgCl, and reversible grayish-white-to-blue transition was observed during a forward and reverse potential sweep. The onset potential for coloration is shifted to higher potential, and that for decoloration is shifted to a lower potential region, as shown in Figure 6. The change in the potential window and onset potential is due to the metallic seed layer. The CA results of Ti-NTO showed that there is an improvement in the reversibility and coloration efficiency compared to bare NTO. But at the same time, the switching time is slightly decreased. The Nb-NTO films are working in the potential range between −2 and 1 V vs Ag/AgCl. The onset potentials of both cathodic and anodic peaks are decreased compared to bare NTO, but it is observed that the peak current is increased. The CA studies showed that the coloration efficiency and reversibility increased by eight times. The incorporation of the NbTi mixed metal layer into the NTO films led to a decrease in reversibility and efficiency. The addition of the seed layer plays an important role in the electrochromic efficiency of the film, and the metallic layer increases the conductivity of the surface, which significantly increases the efficiency of the electro-

chromic performance.[33] Normally, the electrochromic materials are semiconductors in nature, which are coated onto a FTO or ITO substrate by adding a seed layer (metallic layer), which triggers the semiconductors. Also, the metal−metal oxide interface plays a role in enhancing the efficiency of the electrochromic performance of the fabricated thin films. To check the state of the art, a comparison table is shown, which clearly shows the novel EC Nb-NTO film in terms of coloration efficiency, optical contrast, switching coloring and bleaching times, optical memory, etc., which were compared with the states of Nb_2O_5 and TiO_2. The fabricated Nb-NTO film in this work shows higher efficiency than the other reported samples in the way of coloration time, bleaching time, reversibility, and electrochromic efficiency, which are clearly shown in the table, proving our work's efficiency.

3.3. Optical Studies. 3.3.1. Optical Band Gap Studies. The optical band gap energy of pristine films is calculated from UV data by using the Tauc plot (eq 1), which is as follows

$$\alpha h\nu = A \times (h\nu - E_g)^m \tag{1}$$

where α is the absorbance coefficient, h is Planck's constant, ν is the frequency of the incident radiation, A is the absorption edge width parameter, E_g is the material's band gap, and m is the exponent value, which is helpful in finding the transition type. It can take values like 1/2, 3/2, 2, and 3. If the Tauc plot fits with greater accuracy using the m value of 1/2, then the material should be a direct allowed transition type. If the plot is fit with the m value of 3/2, then it is said to be the direct
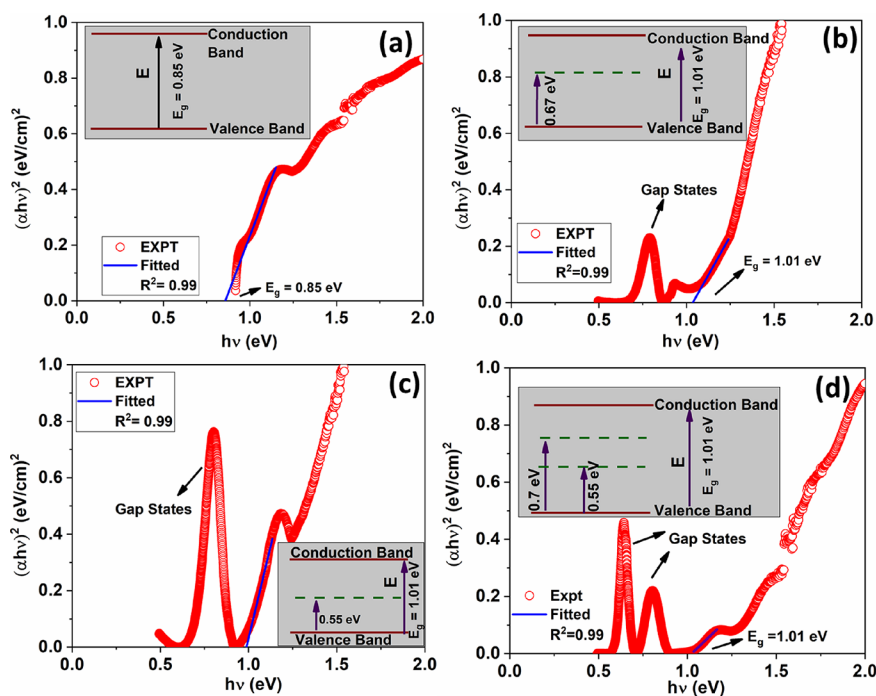
Figure 7. Optical band gap and energy level diagram of (a) bare NTO, (b) Nb-NTO, (c) Ti-NTO, and (d) NbTi-NTO.
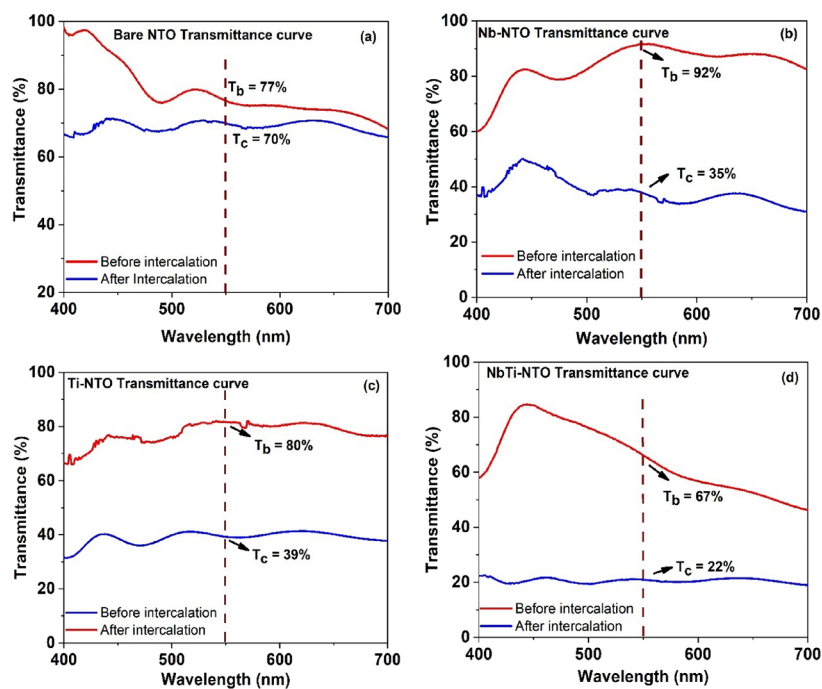

Figure 8. Transmittance spectrum of (a) NTO, (b) Nb-NTO, (c) Ti-NTO, and (d) NbTi-NTO before and after Li$^+$ intercalation.

forbidden transition. The same for $m = 2$ is the indirect allowed transition, and that for $m = 3$ is the indirect forbidden transition. The band gap of bare NTO was calculated using the Tauc plot, and it is shown in Figure S9, in which the plot was well fitted with two m values, viz., $m = 1/2$ (Figure S9a) and $m = 2$ (Figure S9b). This confirmed that the bare NTO film possesses both direct and indirect allowed transitions. The measured direct band gap is about 0.85 eV, and the indirect band gap is about 1.34 eV. So, to find the exact type of transition present in the film, the Urbach energy plot is carried out. This plot helps us to confirm which transition type

dominated in the sample if the Tauc plot fitted with more than one m values. The Urbach energy plot of bare NTO is shown in Figure S9c. This plot clearly showed that the bare NTO films are direct band gap semiconductors with a band gap of about 0.85 eV.

The effect of introducing a metallic layer (Nb, Ti, and NbTi) in between the substrate and the NTO layer on band gap energy was determined, and the plots are shown in Figure 7 also, in which the schematic representation of energy levels was provided for easy understanding. Figure 7a shows the optical band gap and energy level diagram of the bare NTO
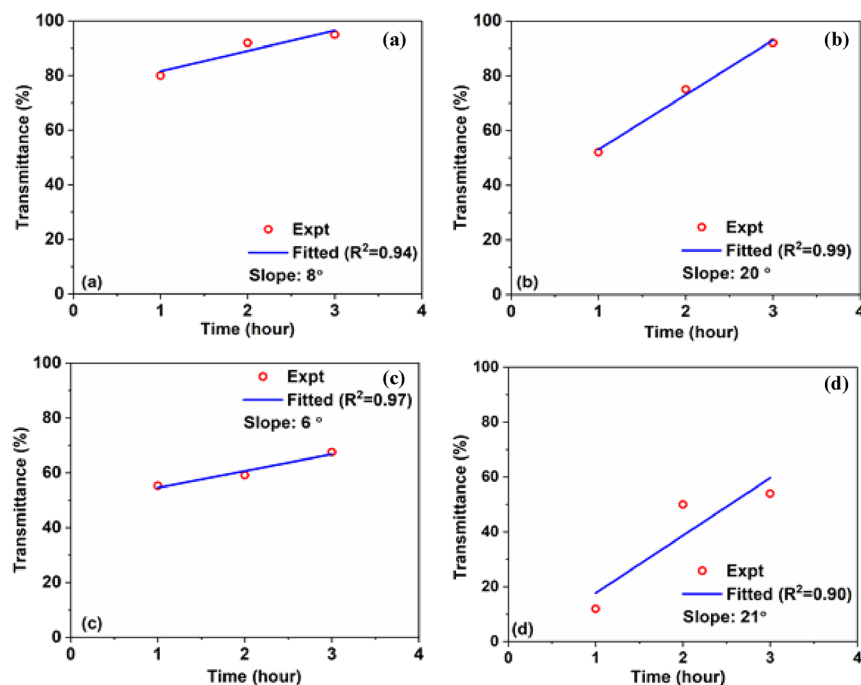
Figure 9. Kinetic studies on rejuvenation of (a) NTO, (b) Nb-NTO, (c) Ti-NTO, and (d) NbTi-NTO films.

film with a band gap value of about 0.85 eV. Introducing a metallic layer increases the band gap energy from 0.85 to 1.01 eV. This is an unexpected one because the metals do not have band gap energy, so introducing a metallic layer in the semiconducting film is expected to reduce the band gap energy. But the reverse happened, which proved that the valence band of bare NTO films was highly affected by the introduction of a thin metallic seed layer. Figure 7b−d shows the optical band gap and energy level diagram of Nb-NTO, Ti-NTO, and NbTi-NTO films. The introduction of a metallic seed layer increases the band gap, but the values are almost similar for the different metal layers. But interestingly, gap states are observed between the valence band and the conduction band, which are represented in the diagram. Generally, the multiple reflections in the Tauc plot occur due to several reasons like the thickness of the film, nature of transition, etc. Here, in bare NTO, the multiple reflections were obtained in the Tauc plot when plotted with $m = 2$ due to the fact that the material showed direct transition. The plot may be linear and fitted with complete accuracy if it is an indirect transition. Also, the discontinuity at 1.75 eV indicated that bare NTO is a direct band gap semiconductor.

3.3.2. Optical Modulation of Films due to Li$^+$ Intercalation. The optical modulation studies of the films before and after Li$^+$ intercalation and de-intercalation are measured using the UV−Vis spectrum, and they are shown in Figure 8. The optical changes are observed in the films during Li$^+$ intercalation and de-intercalation. Coloration happened during Li$^+$ intercalation, and bleaching occurred during Li$^+$ de-intercalation. The transmittance at the bleached state (T_b) and that at the colored state (T_c) of films at 550 nm are used to calculate the optical modulation of the film before and after Li$^+$ intercalation, and the formula used for calculation is shown in eq 2.[6]

The optical modulation values of all the films are tabulated in Table 1. The pristine NTO film without any metallic layer incorporation showed an optical modulation of about 7%.

Incorporation of the metallic layer of Nb, Ti, and NbTi into the NTO film led to an increase in the value of the optical modulation, and there is a minor increment in the transparency. The transparency may be improved due to an increase in the band gap while introducing the metallic seed layer. Better optical modulation was observed in the Nb-NTO film, which was about 57%.

$$\text{optical modulation}(\Delta) = T_b - T_c \qquad (2)$$

3.3.2.1. Galvanostatic Rejuvenation. The electrochemical results suggested that a better EC efficiency of 72.01 cm^2/C with 86% reversibility was observed in the Nb-NTO films. Further, the optical studies also suggested enhanced optical modulation in Nb-NTO films. These results motivated us to do an in-depth analysis of the Nb-NTO film to understand the physical and chemical properties of the film. So, further analyses were carried out for Nb-NTO alone, and in some places, the comparative studies of all four films are presented, which are necessary to understand the properties clearly.

The stability of the film, a significant property for industrial application, by the cycling test was carried out. The Nb-NTO film is subjected to prolonged cycling of about 500 cycles with a 200 mV s^{-1} high scan rate. The cyclic voltammogram of the Nb-NTO film with 500 cycles is shown in Figure S10, which clearly shows that the pattern of the oxidation and reduction peaks was not altered, but the current density was reduced for an increase in the number of cycles. This is due to the film lacking 100% reversibility. Resulting Table 1 showed that the Nb-NTO film possesses 86% reversibility, so the intercalated Li$^+$ cannot be ejected out 100% during the reverse potential scan. The remaining ions were trapped in the film. So, large numbers of ions were trapped inside the film during prolonged cycling. Wen et al.[16] reported that the host surface consisted of two kinds of sites: deep site and shallow site; a high-energy barrier surrounded the deep site, and the shallow site contained a low-energy barrier. The ions trapped inside the deep site cannot be taken out due to the immobility of the

ions. But in the shallow sites, the ions, once trapped, can be regained from the host surface. So, attempts are made to eject the trapped ions from the film, which is called detrapping. For this, galvanostatic rejuvenation was carried out for Nb-NTO films, and the results are shown in Figure S11. The Nb-NTO film requires 20 h to rejuvenate completely. The cyclic voltammogram of the Nb-NTO film before and after 500 cycles and after rejuvenation is shown in Figure S12, which clearly indicates that a prolonged cycle leads to a decrease in current density.

After galvanostatic rejuvenation by applying a constant current of ~2 × 10⁻⁵ A cm⁻² for a period of 20 h, the film recovers to its original state, which is shown in Figure S12. After the ions are trapped from the host surface, the open-circuit potential shifts to nearly equal to the original position and the cyclic voltammetry curve returns back to nearly equal to the original position; this shows the successful rejuvenation of the ions from the host surface.

The rejuvenation kinetics of all films were studied by recording the film optical transmittance spectra for every hour of galvanostatic rejuvenation. The transparency of the film will be recovered and approach its initial as-prepared state due to the detrapping of ions. The results of the rejuvenation kinetic study of all four films are shown in Figure 9, and the original transmittance spectrum is shown in Figure S13. This result showed that the Nb-NTO film rejuvenates at a faster rate than other films. It showed a linear response (Figure 9b) with a slope of 20°. These results strongly proved that the seed layer incorporation strongly affected the electrochromic properties of the film.

EIS analysis was carried out to check the capacitive and resistance nature of the device; still, the fabricated device shows more capacitive nature than resistance nature. The corresponding EIS spectrum is shown in Figure S14 in the Supporting Information, and Ti-NTO, NbTi-NTO, and NTO films showed high R_{ct} values of 46.6 Ω, 81.5 Ω, and 93.7 Ω, respectively, because of the high-resistance nature of the film. Nb-NTO required a less R_{ct} value of 24.2 Ω, which was in good agreement with the EC performance; Nb-NTO showed better performance than other fabricated films.

3.3.2.2. Solid-State Electrochromic Device Fabrication. To commercialize the Nb-NTO electrode for future application, we successfully fabricated the EC device and the color change. After the successful formation of the device in a sandwich model, as shown in Figure 1, the color change of the electrode was tested using cyclic voltammetry analysis and the corresponding EIS was taken for the device. It was observed from the cyclic voltammetry analysis that the fabricated film shows coloration from transparent to blue.

To check the robustness of the fabricated device, it was subjected to a cycling stability test at the scan rate of 100 mV s⁻¹ with a potential window of −2.2 to 1 V for 500 cycles. The fabricated device was still stable, and the current density of the cyclic voltammetry was decreased less after the stability test. This result shows the robustness of the fabricated device, and it will be commercialized for future applications.

4. CONCLUSIONS

In this work, ion-assisted pulsed DC unbalanced confocal magnetron sputtering was used to successfully fabricate the thin films of NTO, Nb-NTO, Ti-NTO, and NbTi-NTO. The layer-by-layer (LBL) strategy was used to improve the efficiency of the electrochromic window. The fabricated films were analyzed with various physical characterizations using XRD, FESEM, Raman, UV−Vis, AFM, HRTEM, XPS, and electrochemical studies. The structural analysis of the Nb-NTO film showed a tetragonal nanocrystalline structure, which fused to form the grains. Raman and XPS results showed that seed layer incorporation much affected the band structure of the film materials and paved the way for Nb-NTO, a favorable condition for better EC material. All the films showed grayish-white-to-blue transition, among which Nb-NTO showed better EC responses with 86% reversibility, good coloration efficiency, and better stability. The effect of introducing a metallic layer (Nb, Ti, and NbTi) in between the substrate and the NTO layer was determined. The band gap energy was calculated, and the metallic seed layer increased the band gap, but the values were almost similar for different metal layers. To check the stability of the film, the Nb-NTO film is subjected to prolonged cycling of about 500 cycles with the scan rate of 200 mV s⁻¹, which is significant for industrial applications. Galvanostatic rejuvenation is carried out for Nb-NTO films, and the film requires 20 h to rejuvenate completely.

■ ASSOCIATED CONTENT

ⓢ Supporting Information

The Supporting Information is available free of charge at https://pubs.acs.org/doi/10.1021/acsomega.2c02716.

> Schematic representation; physical characterizations like XRD and Raman analysis and surface characteristics like FESEM and AFM analysis; XPS deconvoluted spectra; Tauc plot obtained from the UV−Vis spectrum; transmission spectrum and electrochemical results like CV, stability studies, CV studies before and after cycling and after galvanostatic rejuvenation, and galvanostatic rejuvenation studies; EIS spectrum (PDF)
>
> Video S1: three-electrode configuration (MP4)
>
> Video S2: two-electrode configuration (MP4)

■ AUTHOR INFORMATION

Corresponding Author

Balasubramanian Subramanian − *CSIR−Central Electrochemical Research Institute, Karaikudi, Tamilnadu 630 003, India; Academy of Scientific and Innovative Research (AcSIR), Ghaziabad 201 002, India;* ⓘ orcid.org/0000-0003-3329-4298; Phone: +91 4565 241538; Email: bsmanian@cecri.res.in; Fax: +914565 227713

Authors

Karunanithi Balamurugan − *CSIR−Central Electrochemical Research Institute, Karaikudi, Tamilnadu 630 003, India; Academy of Scientific and Innovative Research (AcSIR), Ghaziabad 201 002, India*

Sacratees Santhosh − *CSIR−Central Electrochemical Research Institute, Karaikudi, Tamilnadu 630 003, India; Academy of Scientific and Innovative Research (AcSIR), Ghaziabad 201 002, India; Department of Physics, Government College of Engineering, Krishnagiri, Tamilnadu 635001, India*

Mahendran Mathankumar − *CSIR−Central Electrochemical Research Institute, Karaikudi, Tamilnadu 630 003, India; Academy of Scientific and Innovative Research (AcSIR), Ghaziabad 201 002, India*

Complete contact information is available at:
https://pubs.acs.org/10.1021/acsomega.2c02716

REFERENCES

(1) Khandelwal, H.; Schenning, A. P. H. J.; Debije, M. G. Infrared Regulating Smart Window Based on Organic Materials. *Adv. Energy Mater.* **2017**, DOI: 10.1002/aenm.201602209.

(2) Wang, Y.; Runnerstrom, E. L.; Milliron, D. J. Switchable Materials for Smart Windows. *Annu. Rev. Chem. Biomol. Eng.* **2016**, 1−22, DOI: 10.1146/annurev-chembioeng-080615-034647.

(3) Baetens, R.; Jelle, B. P.; Gustavsen, A. Properties, Requirements and Possibilities of Smart Windows for Dynamic Daylight and Solar Energy Control in Buildings : A State-of-the-Art Review. *Sol. Energy Mater. Sol. Cells* **2010**, *94*, 87−105.

(4) Niklasson, G. A.; Granqvist, C. G. Electrochromics for Smart Windows: Thin Films of Tungsten Oxide and Nickel Oxide , and Devices Based on These. *J. Mater. Chem.* **2007**, 127−156.

(5) Cai, G.; Eh, A. L.; Ji, L.; Lee, P. S. Recent Advances in Electrochromic Smart Fenestration. *Adv. Sustainable Syst.* **2017**, *1*, 1700074.

(6) Santhosh, S.; Mathankumar, M.; Selva Chandrasekaran, S.; Nanda Kumar, A. K.; Murugan, P.; Subramanian, B. Effect of Ablation Rate on the Microstructure and Electrochromic Properties of Pulsed-Laser-Deposited Molybdenum Oxide Thin Films. *Langmuir* **2017**, *33*, 19−33.

(7) Li, R.; Ma, X.; Li, J.; Cao, J.; Gao, H.; Li, T.; Zhang, X.; Wang, L.; Zhang, Q.; Wang, G.; Hou, C.; Li, Y.; Palacios, T.; Lin, Y.; Wang, H.; Ling, X. Flexible and High-Performance Electrochromic Devices Enabled by Self-Assembled 2D TiO$_2$/MXene Heterostructures. *Nat. Commun.* **2021**, 1−11.

(8) Ivanova, T.; Bodurov, G. K. Technologies for Deposition of Transition Metal Oxide Thin Films : Application as Functional Layers in ″Smart Windows″ and Photocatalytic Systems. In *Journal of Physics: Conference Series*; IOP Publishing: 2016, DOI: 10.1088/1742-6596/682/1/012011.

(9) Liu, Y.; Zhao, G.-J.; Zhang, J.-X.; Bai, F.-Q.; Zhang, H.-X. Applied Surface Science First-Principles Investigation on the Interfacial Interaction and Electronic Structure of BiVO$_4$/WO$_3$ Heterostructure Semiconductor Material. *Appl. Surf. Sci.* **2021**, *549*, No. 149309.

(10) Guo, H.; Niu, H.-Y.; Liang, C.; Niu, C.-G.; Huang, D.-W.; Zhang, L.; Tang, N.; Yang, Y.; Feng, C.-Y.; Zeng, G.-M. Insight into the Energy Band Alignment of Magnetically Separable Ag$_2$O/ZnFe$_2$O$_4$ p-n Heterostructure with Rapid Charge Transfer Assisted Visible Light Photocatalysis. *J. Catal.* **2019**, *370*, 289−303.

(11) Xu, Q.; Zhang, L.; Yu, J.; Wageh, S.; Al-ghamdi, A. A.; Jaroniec, M. Direct Z-Scheme Photocatalysts: Principles, Synthesis, and Applications. *Mater. Today* **2018**, *21*, 1042.

(12) Opoku, A. F.; Govender, K. K.; Catharina, G.; Van Sittert, E.; Poomani, P. Insights into the Photocatalytic Mechanism of Mediator-Free Direct Z-Scheme g-C$_3$N$_4$/Bi$_2$MoO$_6$(010) and g-C3N4/Bi2WO6(010) Heterostructures: A Hybrid Density Functional Theory Study. *Appl. Surf. Sci.* **2017**, *6*, 487.

(13) Fes, C.; Wang, W. *Dalton Trans.* **2020**, 13352−13358.

(14) Zhang, S.; Guo, M.; Song, S.; Zhan, K.; Yan, Y.; Yang, J.; Zhao, B. Hierarchical Mo-Doped CoP$_3$ Interconnected Bifunctional Electrocatalyst for Water Splitting In. *Dalton Trans.* **2020**, 5563−5572.

(15) Atak, G.; Bayrak Pehlivan, İ.; Montero, J.; Granqvist, C. G.; Niklasson, G. A. Electrochromic Tungsten Oxide Films Prepared by Sputtering: Optimizing Cycling Durability by Judicious Choice of Deposition Parameters. *Electrochim. Acta* **2021**, *367*, No. 137233.

(16) Wen, R. T.; Granqvist, C. G.; Niklasson, G. A. Eliminating Degradation and Uncovering Ion-Trapping Dynamics in Electrochromic W. O.$_3$ Thin Films. *Nat. Mater.* **2015**, *14*, 996−1001.

(17) Cai, G.; Wang, J.; Lee, P. S. *Next-Generation Multifunctional Electrochromic Devices. Acc. Chem. Res.* 2016, 1469, DOI: 10.1021/acs.accounts.6b00183.

(18) Richardson, J. J.; Cui, J.; Björnmalm, M.; Braunger, J. A.; Ejima, H.; Caruso, F. Innovation in Layer-by-Layer Assembly. *Chem. Rev.* **2016**, *116*, 14828−14867.

(19) Guo, W.; Shim, K.; Kim, Y.-T. Applied Surface Science Ag Layer Deposited on Zn by Physical Vapor Deposition with Enhanced CO Selectivity for Electrochemical CO$_2$ Reduction. *Appl. Surf. Sci.* **2020**, *526*, No. 146651.

(20) Pu, X.; Zhao, D.; Fu, C.; Chen, Z.; Cao, S.; Wang, C.; Cao, Y. Understanding and Calibration of Charge Storage Mechanism in Cyclic Voltammetry Curves. *Angew. Chem., Int. Ed.* **2021**, *60*, 21310−21318.

(21) Tsai, W.; Wang, R.; Boyd, S.; Augustyn, V.; Balke, N. *Nano Energy* **2020**, No. 105592.

(22) Delgado, D.; Concepción, P.; Trunschke, A.; López Nieto, J. M. Tungsten−Niobium Oxide Bronzes: A Bulk and Surface Structural Study. *Dalton Trans.* **2020**, 13282−13293.

(23) Wang, J.; Liu, X.-A.; Zhang, D.; Tong, Z.; Ji, H.; Qu, H.-Y. Zn 2 + Intercalation / de - Intercalation - Based Aqueous Electrochromic Titanium Dioxide Electrode with Zn - Ion Storage. *Ionics* **2021**, 4429, DOI: 10.1007/s11581-021-04182-y.

(24) Krige, A.; Ramser, K.; Sjöblom, M.; Christakopoulos, P.; Rova, U. A New Approach for Evaluating Electron Transfer Dynamics by Using In Situ Resonance Raman Microscopy and Chronoamperometry in Conjunction with a Dynamic Model. *Appl. Environ. Microbiol.* **2020**, *86*, e01535-20.

(25) Zhou, K.; Wang, H.; Liu, J. Coloration and Ion Insertion Kinetics Study in Electrochromic W.O.$_3$ Films by Chronoamperometry. *Int. J. Electrochem. Sci.* **2020**, *15*, 7821−7832.

(26) Lindström, H.; Södergren, S.; Solbrand, A.; Rensmo, H.; Hjelm, J.; Hagfeldt, A.; Lindquist, S.-E. Li + Ion Insertion in TiO$_2$ (Anatase). 1 . Chronoamperometry on CVD Films and Nanoporous Films. *J. Phys. Chem. B* **1997**, *101*, 7710−7716.

(27) Yb, B.; Hydration, O.; Yoo, H.; Kim, J.; Lee, C. Electrical Conductivity Relaxations and Chemical Diffusivities of Electrical Conductivity Relaxations and Chemical Diffusivities of Ba-Ce$_{0.95}$Yb$_{0.05}$O$_{2.975}$ upon Hydration and Oxidation. *J. Electrochem. Soc.* **2009**, B66.

(28) Kim, T.; Choi, W.; Shin, H.-C.; Choi, J.-Y.; Kim, J. M.; Park, M.-S.; Yoon, W.-S. Applications of Voltammetry in Lithium Ion Battery Research. *J. Electrochem. Sci. Technol.* **2020**, *11* (), 14−25, DOI: 10.33961/jecst.2019.00619.

(29) Elgrishi, N.; Rountree, K. J.; McCarthy, B. D.; Rountree, E. S.; Eisenhart, T. T.; Dempsey, J. L. A Practical Beginner's Guide to Cyclic Voltammetry. *J. Chem. Educ.* **2018**, *95*, 197−206.

(30) Wang, H.; Sayed, S. Y.; Luber, E. J.; Olsen, B. C.; Shirurkar, S. M.; Venkatakrishnan, S.; Tefashe, U. M.; Farquhar, A. K.; Smotkin, E. S.; McCreery, R. L.; Buriak, J. M. Redox Flow Batteries: How to Determine Electrochemical Kinetic Parameters. *ACS Nano* **2020**, *14*, 2575−2584.

(31) Mathankumar, M.; Anantharaj, S.; Nandakumar, A. K.; Kundu, S.; Subramanian, B. Potentiostatic phase formation of b-CoOOH onpulsed laser deposited biphasic cobalt oxide thinfilm for enhanced oxygen evolution. *J. Mater. Chem. A* **2017**, *5*, 23053.

(32) Thanka Rajan, S.; Nanda Kumar, A. K.; Subramanian, B. *Nanocrystallization in magnetron sputtered Zr−Cu−Al−Ag thin film metallic glasses CrystEngComm*, 2014, 16,2835, DOI: 10.1039/C3CE42294A.

(33) Mathankumar, M.; Karthick, K.; Nanda Kumar, A. K.; Kundu, S.; Balasubramanian, S. In Situ Decorated Ni Metallic Layer with CoS$_2$-Layered Thin Films via a Layer-by-Layer Strategy Using Pulsed Laser Deposition for Enhanced Electrocatalytic OER. *Inorg. Chem* **2021**, *60*, 8946−8957.

(34) Liu, Y. H.; Fujita, T.; Hirata, A.; Li, S.; Liu, H. W.; Zhang, W.; Inoue, A.; Chen, M. W.Deposition of multicomponent metallic glass films by single-target magnetron sputtering. *Intermetallics21* (**2012**) 105e114, DOI: 10.1016/j.intermet.2011.10.007.